



## Research paper

## Nitrogen photofixation by ultrathin amine-functionalized graphitic carbon nitride nanosheets as a gaseous product from thermal polymerization of urea

Shihai Cao<sup>a</sup>, Huan Chen<sup>a,\*</sup>, Fang Jiang<sup>a,\*</sup>, Xin Wang<sup>b</sup><sup>a</sup> Key Laboratory of Jiangsu Province for Chemical Pollution Control and Resources Reuse, School of Environmental and Biological Engineering, Nanjing University of Science and Technology, Nanjing 210094, China<sup>b</sup> Key Laboratory of Soft Chemistry and Functional Materials, Nanjing University of Science and Technology, Ministry of Education, Nanjing 210094, China

## ARTICLE INFO

## Keywords:

Ultrathin g-C<sub>3</sub>N<sub>4</sub> nanosheets  
Amine-functionalized  
Gaseous polymerization  
Visible-light photocatalysis  
Nitrogen fixation

## ABSTRACT

Amine-functionalized ultrathin graphitic carbon nitride (g-C<sub>3</sub>N<sub>4</sub>) nanosheets were directly obtained by collection of the gaseous thermal polymerization products of urea. The different thermal polymerization mechanisms of urea in the gaseous and solid phases were clarified in this paper. We found that NH<sub>3</sub> was crucial for the formation of g-C<sub>3</sub>N<sub>4</sub> nanosheets in the gaseous phase. The obtained g-C<sub>3</sub>N<sub>4</sub> nanosheets were uniform with a large surface area, high reduction potential, and an enhanced charge-carrier separation rate. Thus, these features might promote the catalytic activity and stability of the material for visible-light photocatalytic nitrogen fixation. Moreover, the one-pot synthesis route to amine-functionalized ultrathin g-C<sub>3</sub>N<sub>4</sub> nanosheets might also be applicable as a new chemical vapor deposition method for deposition of g-C<sub>3</sub>N<sub>4</sub> nanosheets.

## 1. Introduction

Light-driven production of nitrogen from gaseous ammonia has attracted considerable attention because ammonia plays an important role in the development of modern industry and agriculture. Industrial ammonia synthesis, typified by the Haber–Bosch process, requires harsh reaction conditions, including high pressure and high temperature [1–4]. Recently, photocatalytic nitrogen fixation has been considered as an alternative to the Haber–Bosch process. However, the efficiency and stability of catalysts greatly restrict the applications of photocatalytic nitrogen fixation. The development of more abundant, sustainable, and efficient photocatalysts is highly desired.

Graphitic carbon nitride (g-C<sub>3</sub>N<sub>4</sub>), a metal-free visible-light-driven photocatalyst with a narrow band gap of 2.7 eV, has become a promising candidate for photocatalytic nitrogen fixation owing to its widely abundant raw materials, low cost, and simple synthesis method. [5–8] However, bulk g-C<sub>3</sub>N<sub>4</sub> obtained from polycondensation reactions of organic precursors containing carbon and nitrogen (e.g., urea, cyanamide, and dicyandiamide) has many deficiencies, such as a low surface area, limited light harvesting ability, and a high charge carrier recombination rate, which greatly limit its practical applications [9,10]. Morphology modification of g-C<sub>3</sub>N<sub>4</sub> has been reported to be an environmentally friendly and effective route to overcoming its shortcomings. Enlarging the surface area of g-C<sub>3</sub>N<sub>4</sub> and taking advantage of the unique electronic properties of its nanostructures can markedly

improve the photocatalytic performance of the material [11].

The fabrication of g-C<sub>3</sub>N<sub>4</sub> nanosheets is considered to be an effective method for improving its photocatalytic activity [12,13]. The synthesis methods of these materials can be divided into “top-down” and “bottom-up” approaches [14]. The former approach involves the breakdown of bulk g-C<sub>3</sub>N<sub>4</sub> into g-C<sub>3</sub>N<sub>4</sub> nanosheets, based on liquid or thermal exfoliation methods. The latter approach primarily includes template methods, supramolecular preorganization, and solvothermal synthesis [14,15]. Unfortunately, the time consuming multi-step synthesis and low yields of both these approaches limit practical applications of both top-down and bottom-up synthesis methods [8,16]. The development of a simple one-step synthesis of g-C<sub>3</sub>N<sub>4</sub> nanosheets is essential for their wider application. Bulk g-C<sub>3</sub>N<sub>4</sub> is produced by continuous vaporization, decomposition, and copolymerization of carbon-nitrogen precursors [7,12]. Previous reports have focused on polymeric g-C<sub>3</sub>N<sub>4</sub> formed in the solid phase, and there have been few reports on the gaseous products of thermal polymerization. Interestingly, NH<sub>3</sub> is the main product of urea decomposition, which can transfer to the gaseous phase to produce a NH<sub>3</sub>-rich atmosphere. It has been reported that bulk g-C<sub>3</sub>N<sub>4</sub> can be exfoliated into nanosheets by a thermal treatment of bulk g-C<sub>3</sub>N<sub>4</sub> under an NH<sub>3</sub> atmosphere. The NH<sub>3</sub> can intercalate into the interplanar space of bulk g-C<sub>3</sub>N<sub>4</sub>, and break the weak van der Waals bonds between layers of g-C<sub>3</sub>N<sub>4</sub> [17]. It has been proposed that g-C<sub>3</sub>N<sub>4</sub> nanosheets may form in situ in the gaseous phase of a NH<sub>3</sub>-rich atmosphere during the synthesis process of bulk g-C<sub>3</sub>N<sub>4</sub>.

\* Corresponding authors.

E-mail addresses: [hchen404@njust.edu.cn](mailto:hchen404@njust.edu.cn) (H. Chen), [fjiang@njust.edu.cn](mailto:fjiang@njust.edu.cn) (F. Jiang).<http://dx.doi.org/10.1016/j.apcatb.2017.10.028>

Received 24 July 2017; Received in revised form 9 October 2017; Accepted 11 October 2017

Available online 12 October 2017

0926-3373/ © 2017 Elsevier B.V. All rights reserved.

Herein, we used a one-pot approach to obtain amine-functionalized ultrathin g-C<sub>3</sub>N<sub>4</sub> nanosheets by collecting the gaseous products from thermal polymerization of urea at 550 °C (here 550 °C is selected as the preparation temperature of g-C<sub>3</sub>N<sub>4</sub> nanosheets because of g-C<sub>3</sub>N<sub>4</sub> obtained by the pyrolysis of urea at 550 °C has the maximum visible light response and the highest photoactivity) [18]. The g-C<sub>3</sub>N<sub>4</sub> nanosheets possessed a large surface area, photo-generated electrons with a high reduction potential, an increased photoelectric response, and fast charge-carrier separation rate. Moreover, the yield of g-C<sub>3</sub>N<sub>4</sub> nanosheets was approximately 20%, which is much higher than yields reported for air calcination (6%) or H<sub>2</sub>SO<sub>4</sub> exfoliation [7,13]. The photocatalytic activity of the g-C<sub>3</sub>N<sub>4</sub> nanosheets was evaluated by nitrogen photofixation under visible-light irradiation and the photocatalysis mechanism is also discussed.

## 2. Experimental

### 2.1. Preparation of bulk g-C<sub>3</sub>N<sub>4</sub> and g-C<sub>3</sub>N<sub>4</sub> nanosheets

Bulk g-C<sub>3</sub>N<sub>4</sub> and g-C<sub>3</sub>N<sub>4</sub> nanosheets were obtained from thermal polymerization of urea. An open porcelain crucible filled with 20 g of urea was placed into a larger covered porcelain crucible. The two crucibles were heated to 550 °C at a rate of 2 °C/min and maintained at that temperature for 4 h. After cooling down, a light-yellow powder of g-C<sub>3</sub>N<sub>4</sub> nanosheets was finally obtained in the larger porcelain crucible, while bulk g-C<sub>3</sub>N<sub>4</sub> was achieved in the bottom of the small crucible.

### 2.2. Nitrogen photofixation experiments

The nitrogen photofixation experiments were performed in a quartz tube in a XPA-7 photochemical reactor. Briefly, 0.02 g of photocatalyst was added to 50 mL of 4 wt.% aqueous methanol solution. The mixture was stirred in the dark for 30 min to reach a uniform dispersion before a 500 W Xe lamp was turned on and air or N<sub>2</sub> was bubbled at 100 mL/min over the course of the experiment. At certain time intervals during irradiation, 5-mL portions of the suspension were withdrawn and the liquid samples were separated by centrifugation. The concentration of ammonia was determined by the Nessler's reagent spectrophotometry method (JB7478-87) with a UV-2550 spectrophotometer. The nitrogen fixation rate was calculated according to the following equation:

$$y = \frac{\Delta C}{18 \times \Delta t} \times 1000 \quad (1)$$

where  $y$  ( $\mu\text{mol L}^{-1} \text{h}^{-1}$ ) is the nitrogen fixation rate and  $C$  (mg/L) is the concentration of  $\text{NH}_4^+$  at time  $t$ .

### 2.3. Characterization

The urea pyrolysis off-gases were studied by placing 1.0 g of urea into a glass vial, which was then inserted into a tube furnace fitted with a N<sub>2</sub> purge and gas collection adapter, and a thermogravimetric analyzer (Hi-Res TGA 2950). Time of flight mass spectrometer (TOF-MS) identification analysis was carried out using an Autoflex instrument (Bruker Daltonics) operated in the linear positive ion mode using FlexControl 3.3 software. Transmission electron microscope (TEM) images were acquired on a JEOL JEM2100 at an accelerating voltage of 200 kV. Atomic force microscopy (AFM) images were collected by a Model JEM-1400 microscopy system. The specific surface areas were determined by the multipoint Brunauer-Emmett-Teller (BET) method. Powder X-ray diffraction (XRD) patterns were measured by a Bruker D8 Advanced diffraction-meter with Cu K $\alpha$  radiation. Raman spectra were recorded on a microscopic confocal Raman spectrometer (Thermo Electron DXR) with excitation by 785-nm laser light. Fourier transform infrared (FT-IR) spectroscopy was performed on a Nexus 870 spectrometer. Temperature-programmed desorption of CO<sub>2</sub> (CO<sub>2</sub>-TPD) was performed on a TP-5080 multi-functional automatic adsorption

instrument. The content of C, N, O and H was measured by an elemental analyzer (CHN-O-Rapid, Heraeus). X-ray photoelectron spectroscopy (XPS) was performed on a RBD upgraded PHI-5000C ESCA system (Perkin Elmer) with Mg K $\alpha$  radiation ( $h\nu = 1253.6$  eV).

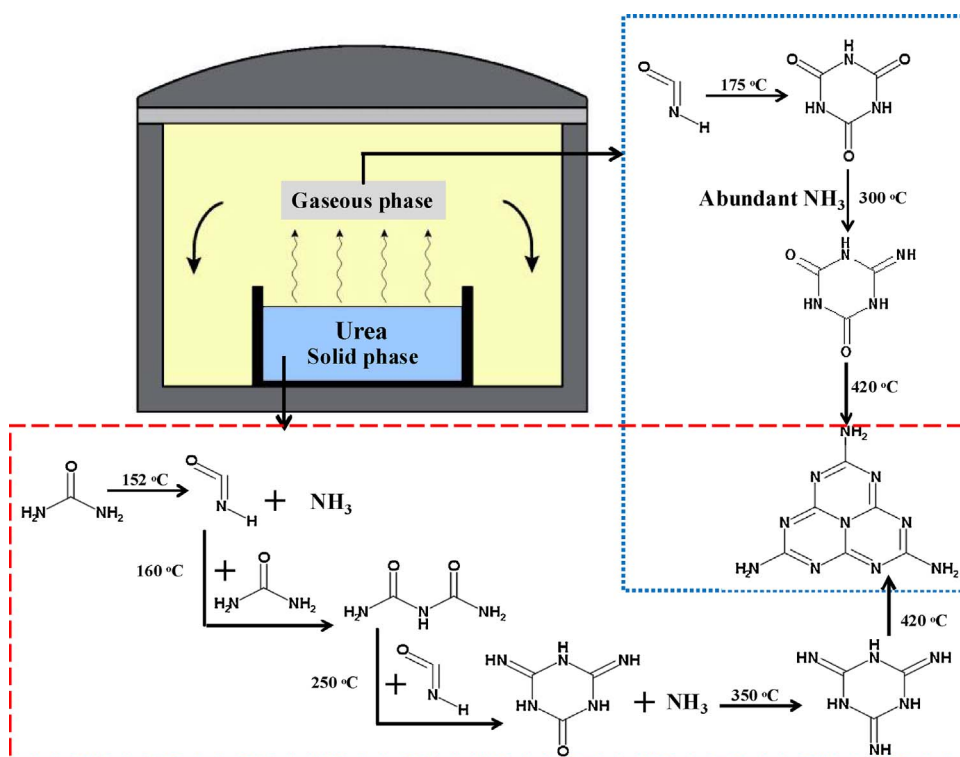
The Schottky curve was obtained on a CHI 660E electrochemical workstation equipped with a standard three-electrode system. A platinum foil was used as the counter electrode and the reference electrode was Ag/AgCl. UV–vis diffuse reflectance spectroscopy was performed on a Hitachi U-3010 UV–vis spectrometer. Photoluminescence spectra (PL) were measured on a Jobin Yvon SPEX Fluorolog-3-P spectrometer. Time-resolved fluorescence decay spectra were recorded on an Edinburgh FLS920 spectrophotometer at an excitation wavelength of 338 nm. The photocurrent transient response was measured on a CHI 660 B electrochemical workstation in a standard three-electrode system. Electron paramagnetic resonance (EPR) spectroscopy was performed on a JEOL JES-FA200 spectrometer.

## 3. Results and discussion

### 3.1. Results of characterization

As previously reported, urea residues formed during thermal copolymerization are found to change from urea to biuret, cyanuric acid, ammelide, ammeline, and melamine as the reaction temperature increased [19]. On the basis of previous reports and laboratory confirmation results, a general scheme for the formation of ultrathin nanosheets is illustrated in Scheme 1. An open porcelain crucible filled with urea was placed into a larger covered porcelain crucible and then heated to 550 °C. Bulk g-C<sub>3</sub>N<sub>4</sub> was produced by continuous vaporization, decomposition and copolymerization of urea [20]. At the beginning of the process (at approximately 152 °C) in the small crucible, the products of urea decomposition filled the entire crucible. These products included cyanic acid and ammonia [ $\text{H}_2\text{N}-\text{CO}-\text{NH}_2 + \text{heat} \rightarrow \text{NH}_3(\text{g}) + \text{HNCO}(\text{g})$ ], as confirmed by the increased intensity of the NCO<sup>−</sup> peak from a FT-IR Si-probe spectra of the melt (Fig. S1). At approximately 160 °C, cyanic acid reacted with intact urea to produce biuret. Then biuret further reacted with cyanic acid to produce cyanuric acid, which then reacted with NH<sub>3</sub> to produce ammelide. As the reaction temperature was increased further, ammeline was obtained by the reaction of ammelide and NH<sub>3</sub>, and then ammeline reacted further with NH<sub>3</sub> to produce melamine [21]. Finally, bulk g-C<sub>3</sub>N<sub>4</sub> was synthesized in a small porcelain crucible via copolymerization of melamine in the solid phase. However, as a product of urea decomposition, cyanic acid can spontaneously and rapidly polymerize to generate cyanuric acid at approximately 175 °C in the gaseous phase [22]. The cyanuric acid then reacts with NH<sub>3</sub> to produce ammelide, and melamine is obtained by the further reaction of ammelide and NH<sub>3</sub>. This reaction route is supported by the increase in the intensity of peaks unique to cyanuric acid at 1058 cm<sup>−1</sup> and ammelide, at 977 cm<sup>−1</sup>, in the FT-IR Si-probe spectra (Fig. S1a). Moreover, TOF-MS was also carried out to confirm the compounds yielded during the thermal pyrolysis. As shown in Fig. S1b, it is clear that the cyanuric acid ( $m/z = 128.0$ ), ammelide ( $m/z = 126.8$ ) and melamine ( $m/z = 124.9$ ) were formed during thermal copolymerization of urea, which was consistent with the results of FT-IR Si-probe spectra. As a small and polar molecule, the large amount of NH<sub>3</sub> formed intercalated into the interplanar space of the melamine, breaking the weak van der Waals bonds during the copolymerization process of melamine in the gaseous phase. The gaseous products fell down into the crucibles as the temperature decreased. Finally, ultrathin g-C<sub>3</sub>N<sub>4</sub> nanosheets were obtained in the larger porcelain crucible and the yield (mass ratio of g-C<sub>3</sub>N<sub>4</sub> nanosheets in total production) was approximately 20%.

The morphology of the bulk g-C<sub>3</sub>N<sub>4</sub> and g-C<sub>3</sub>N<sub>4</sub> nanosheets was investigated by TEM observations and the results are shown in Fig. 1. Compared with the dense and stacked sheets of bulk g-C<sub>3</sub>N<sub>4</sub> (Fig. 1a), the nanosheets showed thin almost transparent features (Fig. 1b).



**Scheme 1.** The different formation processes of g-C<sub>3</sub>N<sub>4</sub> in gaseous and solid phase.

Notably, ultrathin and uniform g-C<sub>3</sub>N<sub>4</sub> nanosheets could be achieved over a large area by gaseous polymerization of urea (Fig. 1c). We used AFM to measure the thickness of the g-C<sub>3</sub>N<sub>4</sub> nanosheets (Fig. 1d). The thickness of individual g-C<sub>3</sub>N<sub>4</sub> nanosheets was approximately 2.0 nm, which corresponds to approximately six atomic layers [8,9]. Furthermore, the BET surface area of the g-C<sub>3</sub>N<sub>4</sub> nanosheets was 90.2 m<sup>2</sup> g<sup>−1</sup>, which was 2.6 times as high as that of bulk g-C<sub>3</sub>N<sub>4</sub> (35.3 m<sup>2</sup> g<sup>−1</sup>), supporting the results of TEM and AFM.

Fig. 2a shows XRD patterns of the bulk g-C<sub>3</sub>N<sub>4</sub> and g-C<sub>3</sub>N<sub>4</sub> nanosheets. The spectra of the g-C<sub>3</sub>N<sub>4</sub> nanosheets contained two peaks that were shared with bulk g-C<sub>3</sub>N<sub>4</sub>, suggesting that the original atomic structure of bulk g-C<sub>3</sub>N<sub>4</sub> was largely retained. The strong peak at approximately 27.4° indexed as (002) represents the interlayer stacking of

aromatic systems [23]. The other weak characteristic peak at 13.1° was indexed as (100) and represents an in-plane structural packing motif. The (002) reflection peak for bulk g-C<sub>3</sub>N<sub>4</sub> at 27.3° shifted to 27.7° for the g-C<sub>3</sub>N<sub>4</sub> nanosheets, corresponding to a decrease of the interlayer stacking distance *d* from 0.325 to 0.322 nm. This shift is related to the nanoscale layer structures of the g-C<sub>3</sub>N<sub>4</sub> nanosheets [24]. The overall diffraction intensities of the g-C<sub>3</sub>N<sub>4</sub> nanosheets became weaker and broader, which was attributed to the reduced layer thickness and was consistent with the AFM results [24].

To further study the structure alteration between the bulk g-C<sub>3</sub>N<sub>4</sub> and g-C<sub>3</sub>N<sub>4</sub> nanosheets, Raman spectra were measured and these results are shown in Fig. 2b. As expected, Raman spectra of the g-C<sub>3</sub>N<sub>4</sub> nanosheets were similar to those of bulk g-C<sub>3</sub>N<sub>4</sub>, which confirmed the

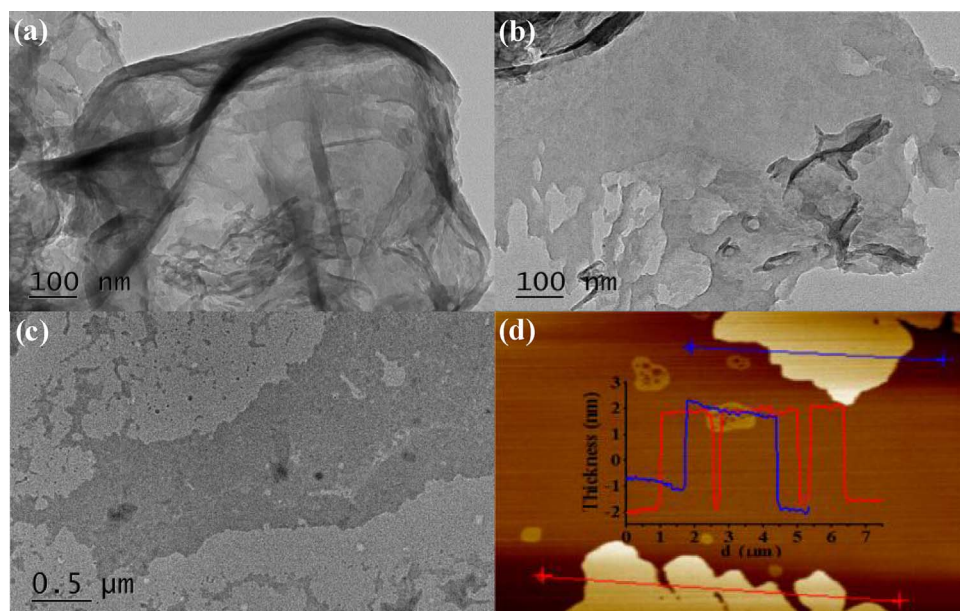


**Fig. 1.** TEM images of (a) bulk g-C<sub>3</sub>N<sub>4</sub> and (b, c) g-C<sub>3</sub>N<sub>4</sub> nanosheets, and (d) AFM images of g-C<sub>3</sub>N<sub>4</sub> nanosheets.

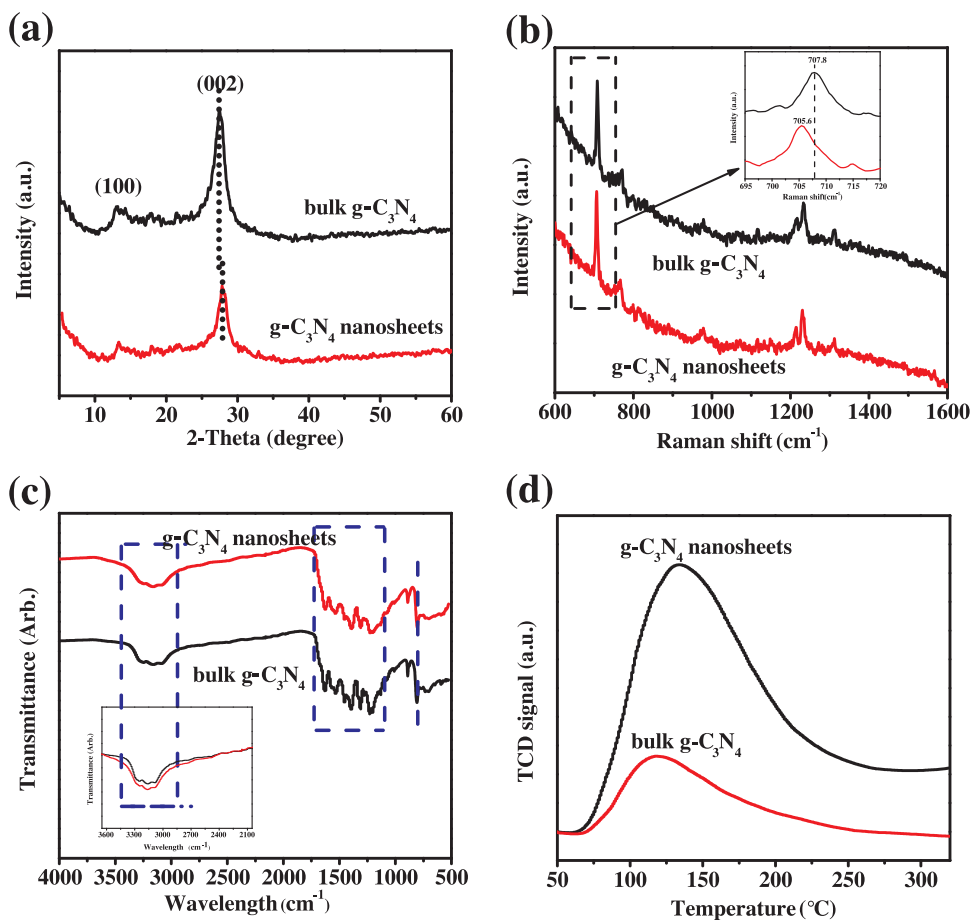


**Fig. 2.** (a) XRD patterns, (b) Raman spectra, (c) FTIR spectra, and (d) CO<sub>2</sub> TPD profiles of bulk g-C<sub>3</sub>N<sub>4</sub> and g-C<sub>3</sub>N<sub>4</sub> nanosheets.

XRD results, and suggested that the g-C<sub>3</sub>N<sub>4</sub> nanosheets retained the crystalline character of the bulk material [25]. Compared with bulk g-C<sub>3</sub>N<sub>4</sub>, the overall diffraction intensities of the g-C<sub>3</sub>N<sub>4</sub> nanosheets became weaker; some structural peaks were difficult to observe, which might be attributed to the shift from the original graphitic-like structure to the new nanoporous structure of the g-C<sub>3</sub>N<sub>4</sub> nanosheets [26]. Notably, the Raman spectra of g-C<sub>3</sub>N<sub>4</sub> nanosheets featured a blue shift of approximately 2 cm<sup>-1</sup>, which could be attributed to the phonon confinement effect, reflecting the ultrathin nature of the g-C<sub>3</sub>N<sub>4</sub> nanosheets [25]. Moreover, the band gap  $E_{(g)}$  of the g-C<sub>3</sub>N<sub>4</sub> nanosheets was estimated from the Raman spectra, according to Eq. (2) [27,28]:

$$I_{(D)}/I_{(G)} = C/E_{(g)}^2 \quad (2)$$

where  $I_{(D)}$  and  $I_{(G)}$  are the relative peak intensities at approximately 1405 cm<sup>-1</sup> and 1570 cm<sup>-1</sup>, respectively, and C is a constant. From the intensity ratio of the D and G bands (Fig. S2), it was clear that the  $E_{(g)}$  of the g-C<sub>3</sub>N<sub>4</sub> nanosheets was larger than that of bulk g-C<sub>3</sub>N<sub>4</sub>. This result was further clarified by UV–vis DRS measurements.

The chemical structures of the surfaces of the bulk g-C<sub>3</sub>N<sub>4</sub> and g-C<sub>3</sub>N<sub>4</sub> nanosheets were characterized by FTIR spectroscopy. As shown in Fig. 2c, the characteristic IR spectrum of the g-C<sub>3</sub>N<sub>4</sub> nanosheets was similar to that of bulk g-C<sub>3</sub>N<sub>4</sub>, demonstrating that the main chemical structures of the two samples were the same. The intense peak at 815 cm<sup>-1</sup> in the g-C<sub>3</sub>N<sub>4</sub> nanosheets corresponded to the vibration of the triazine ring, revealing that tri-s-triazine-based structures were generated through the polymerization of cyanic acid in the gaseous phase [29]. The multiple bands at 1000–1800 cm<sup>-1</sup> were ascribed to the stretching vibration modes of tri-s-triazine heterocyclic stretches. Additionally, the broad band between 3000 and 3600 cm<sup>-1</sup> corresponded to N–H and O–H stretching [30,31]. Note that the transmissivity of the N–H related band in the IR spectrum (inset) of the g-C<sub>3</sub>N<sub>4</sub>

nanosheets was slightly enhanced compared with that of bulk g-C<sub>3</sub>N<sub>4</sub>. This result indicates that a large number of amino groups were introduced onto the surface of the g-C<sub>3</sub>N<sub>4</sub> nanosheets during the polymerization of cyanic acid in the NH<sub>3</sub> atmosphere [17]. To confirm the difference in the content of –NH<sub>2</sub> groups, CO<sub>2</sub>-TPD measurements were conducted on the bulk g-C<sub>3</sub>N<sub>4</sub> and g-C<sub>3</sub>N<sub>4</sub> nanosheets. As shown in Fig. 2d, both samples exhibited a broad peak, which was attributed to strong interactions with basic groups (originating from free –NH<sub>2</sub> groups in g-C<sub>3</sub>N<sub>4</sub>) with slightly acidic CO<sub>2</sub> molecules [32,33]. Compared with bulk g-C<sub>3</sub>N<sub>4</sub>, the CO<sub>2</sub> desorption peak was larger for the g-C<sub>3</sub>N<sub>4</sub> nanosheets confirming that more amino groups were introduced onto the surface of the g-C<sub>3</sub>N<sub>4</sub> nanosheets during the gaseous polymerization of cyanic acid under an NH<sub>3</sub> atmosphere.

The approximate composition of the bulk g-C<sub>3</sub>N<sub>4</sub> and g-C<sub>3</sub>N<sub>4</sub> nanosheets was determined by elemental analysis. As shown in Table S1, the C/N atomic ratio for the g-C<sub>3</sub>N<sub>4</sub> nanosheets was 0.657, which was lower than that of bulk g-C<sub>3</sub>N<sub>4</sub> (0.671). This result indicates that g-C<sub>3</sub>N<sub>4</sub> formed in the gaseous phase was poor in carbon and rich in nitrogen [12].

The compositions and chemical states of the bulk g-C<sub>3</sub>N<sub>4</sub> and g-C<sub>3</sub>N<sub>4</sub> nanosheets were investigated by XPS. As shown in Fig. 3, there were no obvious shifts in the binding energy of the C 1s and N 1s peaks, indicating the presence of the same chemical states in the bulk g-C<sub>3</sub>N<sub>4</sub> and g-C<sub>3</sub>N<sub>4</sub> nanosheets. High-resolution spectra of C 1s, as shown in Fig. 3a, could be fitted by three peaks at 293.6, 288.0, and 284.6 eV, which corresponded to  $\pi$ -excitation, sp<sup>2</sup>-bonded carbon (N=C–N), and aromatic carbon atoms, respectively. In the N 1s spectrum (Fig. 3b), the peak centered at 397.9 eV was attributed to the sp<sup>2</sup>-hybridized nitrogen in s-triazine rings (C–N=C). The peak at 400.0 eV was attributed to N atoms in N-(C)<sub>3</sub> or N atoms bonded with H atoms [34,35]. Additional weak peaks at 400.8 and 404.2 eV could be assigned to amino



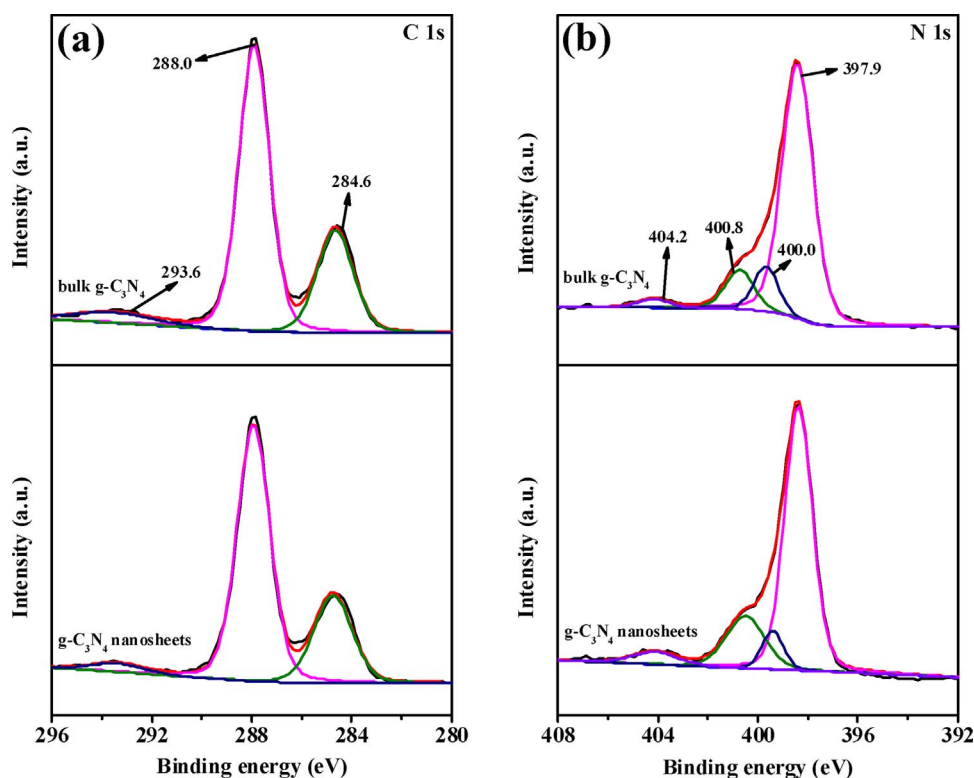


Fig. 3. The high resolution (a) C 1s and (b) N 1s of bulk g-C<sub>3</sub>N<sub>4</sub> and g-C<sub>3</sub>N<sub>4</sub> nanosheets.

functional groups (C–N–H) and  $\pi$ -excitation, respectively [36]. Interestingly, the amount of amino nitrogen in the g-C<sub>3</sub>N<sub>4</sub> nanosheets was higher than that of the bulk g-C<sub>3</sub>N<sub>4</sub> (Table S2). This result also indicates that the g-C<sub>3</sub>N<sub>4</sub> nanosheets possessed more amino groups than bulk g-C<sub>3</sub>N<sub>4</sub>, consistent with the FTIR and CO<sub>2</sub>-TPD results.

The Mott-Schottky plots and UV–vis absorption spectrum were measured to give insights into the electronic band structure of the g-C<sub>3</sub>N<sub>4</sub> nanosheets. As shown in Fig. 4a, the positive slope of the plot suggested that the g-C<sub>3</sub>N<sub>4</sub> nanosheets featured n-type semiconducting properties [37]. Moreover, the flat-band potential for g-C<sub>3</sub>N<sub>4</sub> nanosheets was estimated to be  $-1.56$  eV from the intercept on the abscissa, which was more negative than that of bulk g-C<sub>3</sub>N<sub>4</sub> ( $-1.37$  eV). The UV–vis DRS of the g-C<sub>3</sub>N<sub>4</sub> and g-C<sub>3</sub>N<sub>4</sub> nanosheets are compared in Fig. 4b. The g-C<sub>3</sub>N<sub>4</sub> nanosheets had a clear blue shift of the intrinsic absorption edge compared with that of bulk g-C<sub>3</sub>N<sub>4</sub>, which may be caused by the quantum confinement effect due to the ultrathin properties of g-C<sub>3</sub>N<sub>4</sub> nanosheets. The change in color of the g-C<sub>3</sub>N<sub>4</sub> nanosheets also confirmed that delamination occurred (see inset of Fig. S3). The g-C<sub>3</sub>N<sub>4</sub> nanosheets presented with a lighter yellow color than that of the bulk g-C<sub>3</sub>N<sub>4</sub>. The corresponding band gaps of the bulk g-C<sub>3</sub>N<sub>4</sub> increased from 2.68 to 2.76 eV for the g-C<sub>3</sub>N<sub>4</sub> nanosheets (Fig. S3), as calculated by the Kubelka-Munk method [38]. This result was consistent with the bandgap estimated from the Raman spectra. The larger band gap of the g-C<sub>3</sub>N<sub>4</sub> nanosheets may have resulted from quantum confinement effects of the ultrathin structure of the nanosheets [39,40]. Comprehensive analysis of the band gap and Mott–Schottky plots, enabled the VB edges of bulk g-C<sub>3</sub>N<sub>4</sub> and g-C<sub>3</sub>N<sub>4</sub> nanosheets to be calculated as 1.31 and 1.20 eV, respectively. The VB level of the g-C<sub>3</sub>N<sub>4</sub> nanosheets was 0.11 eV lower than that of the bulk g-C<sub>3</sub>N<sub>4</sub>. The trend of the VB edge downshift was also confirmed in the VB XPS results of the bulk g-C<sub>3</sub>N<sub>4</sub> and g-C<sub>3</sub>N<sub>4</sub> nanosheets, and the VB edges of the g-C<sub>3</sub>N<sub>4</sub> and g-C<sub>3</sub>N<sub>4</sub> nanosheets were 1.34 and 1.25 eV, respectively (Fig. S4).

As shown in Fig. 4c, the PL intensity of the g-C<sub>3</sub>N<sub>4</sub> nanosheets decreased markedly compared with that of bulk g-C<sub>3</sub>N<sub>4</sub>, indicating that radiative recombination of charge carriers was suppressed. The wider

band gap of the g-C<sub>3</sub>N<sub>4</sub> nanosheets was further confirmed by the blue shift of the fluorescence emission spectrum by 10 nm. The charge carrier lifetimes of the bulk g-C<sub>3</sub>N<sub>4</sub> and g-C<sub>3</sub>N<sub>4</sub> nanosheets were measured by time-resolved PL experiments and the results are compared in Fig. 4d. The g-C<sub>3</sub>N<sub>4</sub> nanosheets showed slower decay kinetics compared with those of bulk g-C<sub>3</sub>N<sub>4</sub>, which may be attributed to improved electron transport and/or electronic band structure changes induced by the quantum confinement effect in the nanosheets. According to the fitting calculation, the average carrier lifetimes of the bulk g-C<sub>3</sub>N<sub>4</sub> and g-C<sub>3</sub>N<sub>4</sub> nanosheets were 3.312 and 6.823 ns, respectively. The increased lifetime of charge carriers in the g-C<sub>3</sub>N<sub>4</sub> nanosheets could be attributed to the improved electron transport and electronic band structure changes induced by quantum confinement effects, which enhanced the probability of their participation in the photocatalytic reactions before recombination [41,42].

To reveal the electronic conductivity of the bulk g-C<sub>3</sub>N<sub>4</sub> and g-C<sub>3</sub>N<sub>4</sub> nanosheets, we measured the photocurrent response curves and electrochemical impedance spectroscopy. As shown in Fig. 4e, the photocurrent of the g-C<sub>3</sub>N<sub>4</sub> nanosheets was much higher than that of bulk g-C<sub>3</sub>N<sub>4</sub>, suggesting a faster rate of interfacial charge-transport. This conclusion was also supported by electrochemical impedance spectroscopy (EIS) (Fig. 4f), which clearly showed a smaller arc radius for the g-C<sub>3</sub>N<sub>4</sub> nanosheets than that of the bulk g-C<sub>3</sub>N<sub>4</sub>. This result suggested that the g-C<sub>3</sub>N<sub>4</sub> nanosheets efficiently promoted the separation and transfer of photo-generated charge carriers. Such differences in the electronic conductivity could be explained by the structural properties of the g-C<sub>3</sub>N<sub>4</sub> nanosheets. Specifically, the g-C<sub>3</sub>N<sub>4</sub> nanosheets mainly consisted of large hydrogen-bonded strands of polymeric units, which could act as charge carrier transport channels. Photo-excited charge carriers in bulk g-C<sub>3</sub>N<sub>4</sub> could easily recombine because most of the isolated strands in the layers of the bulk g-C<sub>3</sub>N<sub>4</sub> lacked efficient charge carrier transport channels from the bulk to the surface of the photocatalyst [12].

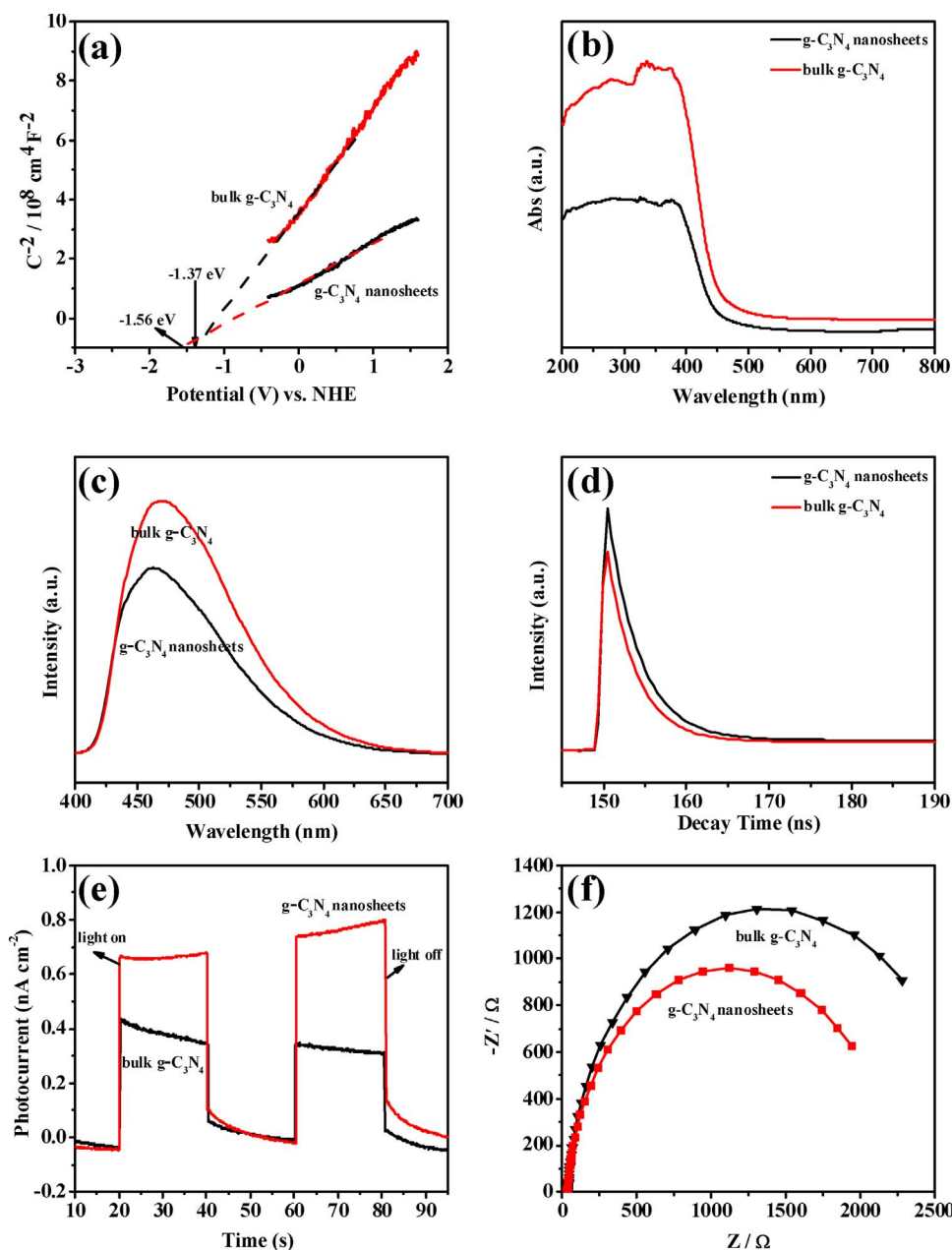


Fig. 4. (a) Mott-Schottky plot, (b) UV-vis absorption spectrum, (c) PL spectra, (d) time-resolved PL spectra, (e) photocurrent transient responses, and (f) EIS Nyquist plots in the dark of bulk  $g\text{-C}_3\text{N}_4$  and  $g\text{-C}_3\text{N}_4$  nanosheets.

### 3.2. Improved photocatalytic activity of $g\text{-C}_3\text{N}_4$ nanosheets

#### 3.2.1. Photocatalytic performance of $g\text{-C}_3\text{N}_4$ nanosheets

The photocatalytic activities of the  $g\text{-C}_3\text{N}_4$  nanosheets were evaluated from their nitrogen photofixation activity under visible-light irradiation. As shown in Fig. 5a, the  $g\text{-C}_3\text{N}_4$  nanosheets exhibited superior photocatalytic activity compared with that of bulk  $g\text{-C}_3\text{N}_4$ . The average nitrogen fixation rate of the  $g\text{-C}_3\text{N}_4$  nanosheets was  $60.5 \mu\text{mol h}^{-1}$ , which was 1.9 times as high as that of bulk  $g\text{-C}_3\text{N}_4$  ( $31.8 \mu\text{mol h}^{-1}$ ). The stabilities of the  $g\text{-C}_3\text{N}_4$  nanosheets as photocatalysts for nitrogen photofixation were evaluated in a recycling experiment with four-cycles. As depicted in Fig. 5b, the  $\text{NH}_4^+$  production increased steadily with irradiation time, while the nitrogen fixation rate exhibited a slight decrease over repeated cycling. This decrease might be attributed to the loss of photocatalyst particles during recycling runs and/or experimental error. As observed in Fig. S5, there were no notable differences in the TEM, FT-IR and XRD spectra of the  $g\text{-C}_3\text{N}_4$  nanosheets after four cycles, suggesting its good chemical and photochemical stability.

#### 3.2.2. Mechanism of nitrogen photofixation

As observed in Fig. 5c, the production of  $\text{NH}_4^+$  during photocatalysis over  $g\text{-C}_3\text{N}_4$  nanosheets decreased in the presence of  $\text{N}_2$ , indicating that  $\text{O}_2$  played a dominant role in the photocatalytic  $\text{N}_2$  fixation by the  $g\text{-C}_3\text{N}_4$  nanosheets. To determine the role of  $\text{O}_2$ , we used a spin-trapping EPR technique based on 5,5-dimethyl-1-pyrroline-*N*-oxide (DMPO). As shown in Fig. 5d, the DMPO/ $\cdot\text{O}_2^-$  characteristic peaks of the  $g\text{-C}_3\text{N}_4$  nanosheets were enhanced, which could be attributed to the greater oxidation ability of the  $g\text{-C}_3\text{N}_4$  nanosheets. The VB potential of the  $g\text{-C}_3\text{N}_4$  nanosheets ( $+1.2 \text{ eV}$  vs. NHE) was more negative than  $E_0(\cdot\text{OH}/\text{OH}^- = +1.99 \text{ eV}$  vs. NHE); hence,  $\cdot\text{OH}$  radicals could not be directly produced by holes and were instead generated by a multistep reaction ( $\text{O}_2^- \rightarrow \text{H}_2\text{O}_2 \rightarrow \cdot\text{OH}$ ) [43,44]. The  $\cdot\text{OH}$  generated could easily react with methanol to form  $\cdot\text{CO}_2^-$ . Moreover,  $\text{CO}_2$  adsorbed to the surface of the  $g\text{-C}_3\text{N}_4$  nanosheets could also generate  $\cdot\text{CO}_2^-$ . The strong reducing ability of  $\cdot\text{CO}_2^-$  ( $E_{\text{CO}_2/\cdot\text{CO}_2^-} = 1.8 \text{ V}$ ) facilitated the fixation of  $\text{N}_2$  to  $\text{NH}_3$  [45].

To illuminate the role of indirect electron transfer induced by  $\cdot\text{CO}_2^-$ , the photocatalytic nitrogen fixation over  $g\text{-C}_3\text{N}_4$  nanosheets

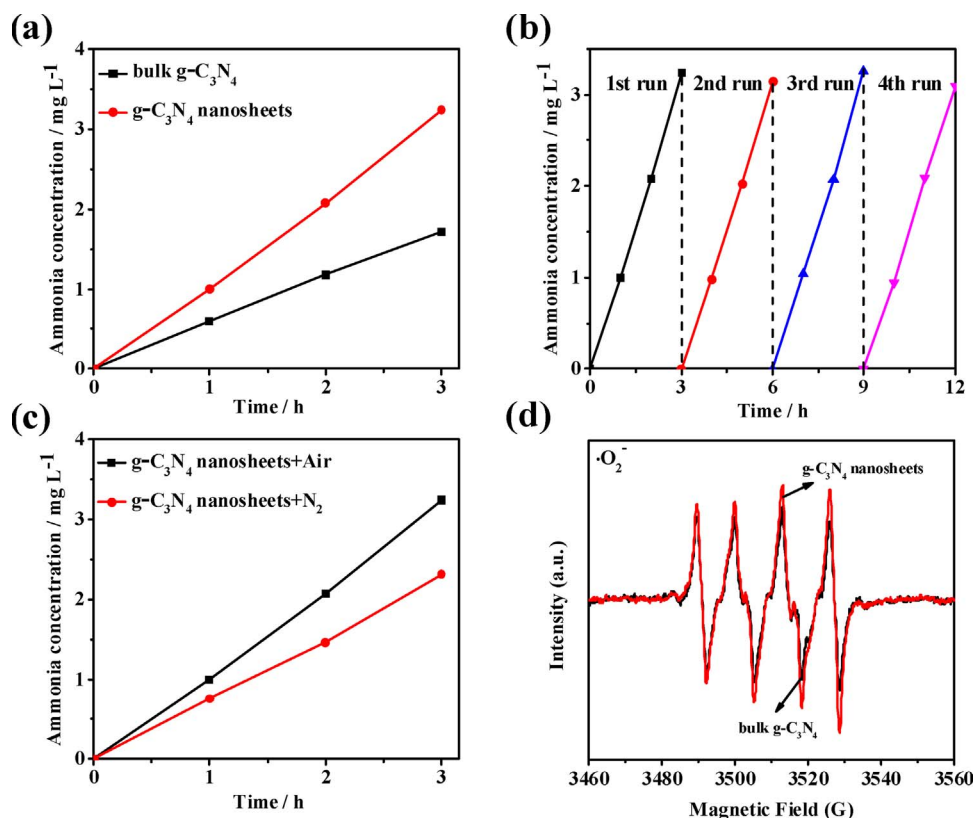
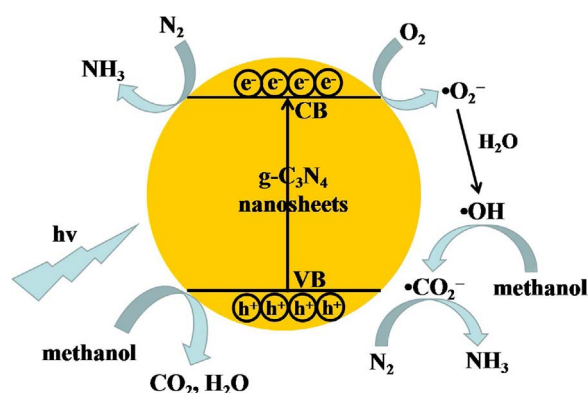
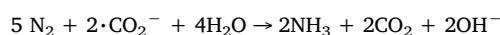
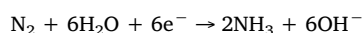
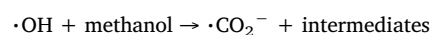
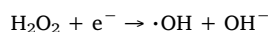
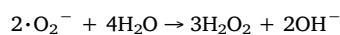
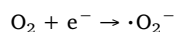
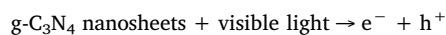


Fig. 5. (a) Visible-light nitrogen fixation over bulk g-C<sub>3</sub>N<sub>4</sub> and g-C<sub>3</sub>N<sub>4</sub> nanosheets. (b) Cycling runs for the visible-light nitrogen fixation over g-C<sub>3</sub>N<sub>4</sub> nanosheets. (c) Visible-light nitrogen fixation under different atmospheres over g-C<sub>3</sub>N<sub>4</sub> nanosheets. (d) DMPO spin-trapping ESR spectra recorded for ·O<sub>2</sub><sup>-</sup> in bulk g-C<sub>3</sub>N<sub>4</sub> and g-C<sub>3</sub>N<sub>4</sub> nanosheets.

was further performed with tertiary butyl alcohol as a hole scavenger. Alcohols with lower  $E_{\text{HOMO}}$  (highest occupied molecular orbital energy) were more easily oxidized, which contributed to an improvement of their catalytic performance [45]. As a sacrificial reagent, methanol can lose electrons more easily, making it more suitable and effective than tertiary butyl alcohol owing to its lower HOMO. However, the photocatalytic N<sub>2</sub> fixation by the g-C<sub>3</sub>N<sub>4</sub> nanosheets was more effective with tertiary butyl alcohol than with methanol (Fig. S6). This result was attributed to the increased rate of formation of ·CO<sub>2</sub><sup>-</sup>, which led to enhancement of the indirect electron transfer rate.

On the basis of these comparative investigations, the enhanced photocatalytic activity of the g-C<sub>3</sub>N<sub>4</sub> nanosheets can be attributed to their large surface area, increased band gap, improved electron transport ability, and the prolonged lifetime of charge carriers, compared with those properties of bulk g-C<sub>3</sub>N<sub>4</sub>. A detailed photocatalytic mechanism is proposed and illustrated in Scheme 2. During the nitrogen photofixation reaction, photogenerated electrons in the CB of g-C<sub>3</sub>N<sub>4</sub> reduce O<sub>2</sub> to ·O<sub>2</sub><sup>-</sup>, and ·OH is generated via a multistep reaction (·

O<sub>2</sub><sup>-</sup> → H<sub>2</sub>O<sub>2</sub> → ·OH) from oxygen. Methanol is then oxidized to ·CO<sub>2</sub><sup>-</sup> by ·OH species, facilitating the reduction of N<sub>2</sub> to NH<sub>3</sub>. Besides, as holes (h<sup>+</sup>) scavenger, methanol can be directly oxidized and promote the charge-carrier separation. Then, N<sub>2</sub> can be activated and transformed into ammonia by a multielectron reduction process on the g-C<sub>3</sub>N<sub>4</sub> nanosheets surface [1]. Possible photocatalytic nitrogen fixation steps are listed as follows:



Scheme 2. The mechanism of photocatalytic nitrogen fixation over g-C<sub>3</sub>N<sub>4</sub> nanosheets.

#### 4. Conclusion

In summary, amine-functionalized ultrathin g-C<sub>3</sub>N<sub>4</sub> nanosheets with improved structural and optoelectronic properties were directly synthesized from urea by a simple one-step separation method. The g-C<sub>3</sub>N<sub>4</sub> nanosheets were achieved in the gaseous phase during the polymerization of the urea, via the reaction of cyanic acid under an NH<sub>3</sub> atmosphere, which greatly improved the yield of the g-C<sub>3</sub>N<sub>4</sub> nanosheets. The synthesized g-C<sub>3</sub>N<sub>4</sub> nanosheets exhibited a large surface area, high reduction potential and enhanced charge-carrier separation rate. Thus, compared with bulk g-C<sub>3</sub>N<sub>4</sub>, the photocatalytic activity and stability of the g-C<sub>3</sub>N<sub>4</sub> nanosheets in nitrogen photofixation reactions under visible-light irradiation were enhanced. The main reactive species in nitrogen photofixation over g-C<sub>3</sub>N<sub>4</sub> nanosheets were e<sup>-</sup> and ·CO<sub>2</sub><sup>-</sup>. The present study provides a low-cost, easily scaled, and

environmental friendly method to prepare g-C<sub>3</sub>N<sub>4</sub> nanosheets, which may lead to wider applications of g-C<sub>3</sub>N<sub>4</sub> nanosheets.

## Acknowledgments

The financial supports from the National Natural Science Foundation of China (Nos. 51478223 and 51678306), China Postdoctoral Science Foundation (2017T100372, 2016M590458 and 2013M541677), the Jiangsu Planned Projects for Postdoctoral Research Funds (1202007B) and the Fundamental Research Funds for the Central University (30915011308) are gratefully acknowledged.

## Appendix A. Supplementary data

Supplementary data associated with this article can be found, in the online version, at <http://dx.doi.org/10.1016/j.apcatb.2017.10.028>.

## References

- [1] S. Sun, X. Li, W. Wang, L. Zhang, X. Sun, *Appl. Catal. B: Environ.* 200 (2017) 323–329.
- [2] P.C. Dos Santos, R.Y. Igarashi, H. Lee, B.M. Hoffman, L.C. Seefeldt, D.R. Dean, *Acc. Chem. Res.* 38 (2005) 208–214.
- [3] A. Banerjee, B.D. Yuhas, E.A. Margulies, Y. Zhang, Y. Shim, M.R. Wasielewski, M.G. Kanatzidis, *J. Am. Chem. Soc.* 137 (2015) 2030–2034.
- [4] T. Shima, S. Hu, G. Luo, X. Kang, Y. Luo, Z. Hou, *Science* 340 (2013) 1549–1552.
- [5] X. Wang, K. Maeda, A. Thomas, K. Takanebe, G. Xin, J.M. Carlsson, K. Domen, M. Antonietti, *Nat. Mater.* 8 (2009) 76–80.
- [6] Y. Wang, X. Wang, M. Antonietti, *Angew. Chem. Int. Ed.* 51 (2012) 68–89.
- [7] W.J. Ong, L.L. Tan, Y.H. Ng, S.T. Yong, S.P. Chai, *Chem. Rev.* 116 (2016) 7159–7329.
- [8] P. Yang, H. Ou, Y. Fang, X. Wang, *Angew. Chem. Int. Ed.* 129 (2017) 4050–4054.
- [9] N. Cheng, J. Tian, Q. Liu, C. Ge, A.H. Qusti, A.M. Asiri, A.O. Al-Youbi, X. Sun, *ACS Appl. Mater. Inter.* 5 (2013) 6815–6819.
- [10] S.W. Cao, J.G. Yu, *J. Phys. Chem. Lett.* 5 (2014) 2101–2107.
- [11] Y. Nishibayashi, M. Saito, S. Uemura, S. Takekuma, H. Takekuma, Z. Yoshida, *Nature* 428 (2004) 279–280.
- [12] P. Niu, L. Zhang, G. Liu, H. Cheng, *Adv. Funct. Mater.* 22 (2012) 4763–4770.
- [13] S. Yang, Y. Gong, J. Zhang, L. Zhan, L. Ma, Z. Fang, R. Vajtai, X. Wang, P.M. Ajayan, *Adv. Mater.* 25 (2013) 2452–2456.
- [14] Y.B. Guo, L. Xu, H.B. Liu, Y.J. Li, C.M. Che, Y.L. Li, *Adv. Mater.* 27 (2015) 985–1013.
- [15] Y. Zheng, L. Lin, B. Wang, X. Wang, *Angew. Chem. Int. Ed.* 54 (2015) 12868–12884.
- [16] F. Cheng, H. Wang, X. Dong, *Chem. Commun.* 51 (2015) 7176–7179.
- [17] P. Xia, B. Zhu, J. Yu, S. Cao, M. Jaroniec, *J. Mater. Chem. A* 5 (2017) 3230–3238.
- [18] J. Liu, T. Zhang, Z. Wang, G. Dawson, W. Chen, *J. Mater. Chem.* 21 (2011) 14398–14401.
- [19] P.M. Schaber, J. Colson, S. Higgins, E. Dietz, D. Thielen, B. Anspach, J. Brauer, *Am. Lab.* 31 (1999) 13–21.
- [20] A.G. Koryakin, V.A. Galperin, V.M. Karlik, L.N. Al'tshuler, A.N. Sarbaev, V.I. Zagranichnyi, *Zh. Org. Khim.* 12 (1976) 977–980.
- [21] P.M. Schaber, J. Colson, S. Higgins, D. Thielen, B. Anspach, J. Brauer, *Thermochim. acta* 424 (2004) 131–142.
- [22] G. Herzberg, C. Reid, *Discuss. Faraday Soc.* 9 (1950) 92–99.
- [23] P. Qiu, H. Chen, C. Xu, N. Zhou, F. Jiang, X. Wang, Y. Fu, *J. Mater. Chem. A* 3 (2015) 24237–24244.
- [24] C. Chang, Y. Fu, M. Hu, C. Wang, G. Shan, L. Zhu, *Appl. Catal. B: Environ.* 142 (2013) 553–560.
- [25] X. Zhang, X. Xie, H. Wang, J. Zhang, B. Pan, Y. Xie, *J. Am. Chem. Soc.* 135 (2012) 18–21.
- [26] J. Xu, Y. Wang, Y. Zhu, *Langmuir* 29 (2013) 10566–10572.
- [27] Y. Zhang, Q. Pan, G. Chai, M. Liang, G. Dong, Q. Zhang, J. Qiu, *Sci. Rep.* 3 (2013) 2163–2170.
- [28] A.C. Ferrari, J. Robertson, *Phys. Rev. B* 61 (2000) 14095–14107.
- [29] J.S. Zhang, Y. Chen, X.C. Wang, *Energy Environ. Sci.* 8 (2015) 3092–3108.
- [30] Q.H. Liang, Z. Li, Z.H. Huang, F.Y. Kang, Q.H. Yang, *Adv. Funct. Mater.* 25 (2015) 6885–6892.
- [31] X.L. Lu, K. Xu, P.Z. Chen, K.C. Jia, S.L. Liu, C.Z. Wu, *J. Mater. Chem. A* 2 (2014) 18924–18928.
- [32] S. Talapaneni, S. Anandan, G. Mane, C. Anand, D. Dhawale, S. Varghese, A. Mano, T. Mori, A. Vinu, *J. Mater. Chem.* 22 (2012) 9831–9840.
- [33] R.D. Richardson, E.J. Holland, B.K. Carpenter, *Nat. Chem.* 3 (2011) 301–303.
- [34] P. Qiu, H. Chen, F. Jiang, *RSC Adv.* 4 (2014) 39969–39977.
- [35] J. Tian, L. Zhang, X. Fan, Y. Zhou, M. Wang, R. Cheng, M. Li, X. Kan, X. Jin, Z. Liu, Y. Gao, J. Shi, *J. Mater. Chem. A* 4 (2016) 13814–13821.
- [36] Y. Wang, X. Wang, M. Antonietti, *Angew. Chem. Int. Ed.* 51 (2012) 68–89.
- [37] S. Chu, Y. Wang, Y. Guo, J. Feng, C. Wang, W. Luo, X. Fan, Z. Zou, *ACS Catal.* 3 (2013) 912–919.
- [38] I. Tsuji, H. Kato, A. Kudo, *Angew. Chem. Int. Ed.* 117 (2005) 3631–3634.
- [39] S.B. Yang, Y.J. Gong, J.S. Zhang, L. Zhan, L.L. Ma, Z.Y. Fang, R. Vajtai, X.C. Wang, P.M. Ajayan, *Adv. Mater.* 25 (2013) 2452–2456.
- [40] L. Shi, K. Chang, H.B. Zhang, X. Hai, L.Q. Yang, T. Wang, J.H. Ye, *Small* 12 (2016) 4431–4439.
- [41] P. Zhang, T. Wang, X.X. Chang, J.L. Gong, *Acc. Chem. Res.* 49 (2016) 911–921.
- [42] T. Hisatomi, K. Takanebe, K. Domen, *Catal. Lett.* 145 (2015) 95–108.
- [43] L. Ye, J. Liu, Z. Jiang, T. Peng, L. Zan, *Appl. Catal. B: Environ.* 142 (2013) 1–7.
- [44] P. Qiu, C. Xu, H. Chen, F. Jiang, X. Wang, R. Lu, X. Zhang, *Appl. Catal. B: Environ.* 206 (2017) 319–327.
- [45] N. Dimitrijevic, B. Vijayan, O. Poluektov, T. Rajh, K. Gray, H. He, P. Zapol, *J. Am. Chem. Soc.* 133 (2011) 3964–3971.